

# **The NASA Infrared Telescope Facility Investigation of Comet Shoemaker-Levy 9 and its Collision with Jupiter: Preliminary Results**

G. Orton, M. A'Hearn, K. Baines, D. Deming, T. Dowling  
J. Goguen, C. Griffith, H. Hammel, W. Hoffmann, J. Hunten  
D. Jewitt, T. Kostiuk, S. Miller, K. Noll, K. Zahnle  
N. Achilleos, A. Dayal, L. Deutsch, F. Espenak, P. Esterle  
J. Friedson, K. Fast, J. Barrington, J. Hera, R. Joseph  
D. Kelly, J. Lacy, C. Lisse, J. Rayner, A. Sprague, M. Shure  
K. Wells, P. Yanamandra-Fisher, D. Zipoy, D. Buhl, W. Golisch  
D. Griep, C. Kaminski, C. Arden, A. Chaikin, J. Goldstein  
D. Gilmore, G. Fazio, T. Kanamori, H. Lam, T. Livengood  
M.-M. MacLow, M. Marley, T. Momary, D. Robertson, P. Romani  
M. Sykes, J. Tennyson, D. Wellnitz, S.-W. Ying  
submitted to *Science*

October 17, 1994

K. Baines is at 183-601, J. D. Goguen is at M.S. 183-501, and J. Friedson, G. Orton, P. Yanamandra-Fisher are at M.S. 169-237, Jet Propulsion Laboratory, California Institute of Technology, 4800 Oak Grove Drive, Pasadena, CA 91109; T. Dowling is at 54-420, J. Barrington at 54-426, and H. Hammel at 54-416, Massachusetts Institute of Technology, Cambridge, MA 02139; W. Golisch, D. Griep, J. Hera, D. Jewitt, R. Joseph, C. Kaminski, J. Rayner, and M. Shure are at the Institute for Astronomy, U. Hawaii, 2680 Woodlawn Drive, Honolulu, HI 96822; M. A'Hearn, P. Esterle, K. Fast, D. Wellnitz, and D. Zipoy are at the Astronomy Dept. University of Maryland, College Park, MD 20742; G. Bjoraker, J. BuM, D. Deming, R. Espenak, T. Kostiuk, T. Livengood, and P. Romani are at Code 693, and C. Lisse is at Code 685, NASA Goddard Space Flight Center, Greenbelt, MD 20771; L. Deutsch is at the Five-College Astronomy Dept., U. Massachusetts, Amherst, MA 01003; A. Dayal and W. Hoffmann are at the Steward observatory, and J. Hunten, A. Sprague, M. Sykes, and K. Wells are at the Lunar and Planetary Lab., Univ. of Arizona, Tucson, AZ 85721; C. Griffith is at the Department of Physics and Astronomy, Northern Arizona University, Flagstaff, AZ 86011-6010; J. Goldstein is at the National Air and Space Museum, Washington, DC 20560; N. Achilleos, H. Lam, S. Miller and J. Tennyson are at the Department of Physics and Astronomy, University College, London, Gower Street, London WC1E 6BT, UK; D. Gilmore and K. Noll are at the Space Telescope Science Institute, 3700 San Martin Drive, Baltimore, MD 21218; K. Zahnle is at 245-3, NASA Ames Research Center, Moffett Field, CA 94035; D. Kelly and J. Lacy are at the Dept. of Astronomy, Univ. of Texas, Austin, TX 78712; C. Arden is at Trinity Hall, Cambridge CB2 1TJ, England; A. Chaikin is at the Dept. of Physics, St. Andrews Univ., Fife, Scotland; G. Fazio is at the Smithsonian Astrophysical Obs., 60 Garden St., Cambridge, MA 02138; T. Kanamori is at the Dept. of Mechanical Engineering and Design, Stanford Univ., Stanford, CA 94305; M. Marley is at the Dept. of Astronomy, New Mexico State Univ., Box 30001 /Dept. 4500, Las Cruces, NM 88003; M.-M. MacLow is at the Dept. of Astronomy and Astrophysics, Univ. of Chicago, 5640 Ellis Ave., Chicago, IL 60637; T. Momary is at 3806 Geology Building, U. C. L. A., 405 Hilgard Ave., Los Angeles, CA 90024-1567; D. Robertson is at the Dept. of Physics and Astronomy, Leicester Univ., University Road, Leicester LE1 7RH, UK; J. Spitale is at Campus Box 972, California Institute of Technology, Pasadena, CA 91126; and S.-W. Ying is at the Imperial College of Science, Technology

and Medicine, Exhibition Road, SW7 2BZ, UK;

## Abstract

The NASA Infrared Telescope Facility investigated the Comet Shoemaker-Levy 9 collision with Jupiter from July 12 to August 7, 1994. Fragment K, undetectable in the near infrared a week before, brightened an hour before impact. Strong thermal infrared emission lasting several minutes was observed after the impacts of fragments C, G and R. All impacts warmed the stratosphere and some the troposphere up to several Kelvins. Stratospheric ammonia increased by 5-50 times or more. Impact-related particles extended vertically to the level of several millibars pressure. The north polar near-infrared aurora brightened by nearly a factor of 5 a week after the impacts.

## Introduction

Many of the extraordinary events surrounding the impact of Comet Shoemaker-Levy 9 with Jupiter were observed from the NASA Infrared Telescope Facility (IRTF) from July 12 to August 7 (UT), 1994, by team selected by peer review (1) and their colleagues. Their science goals included characterizing the behavior of cometary fragments under the influence of Jupiter's electromagnetic environment, measuring meteor and plume radiation, determining changes in and the evolution of atmospheric particulate levels, temperatures, and chemistry at the impact sites, determining whether the ring system changed in the increased dust environment, and searching for atmospheric inertia-gravity waves (8) and internal seismic (7) waves and trapped oscillations (p-modes) induced by the collisions. We will report on the search for and analysis of waves and oscillations elsewhere.

A new Multiple Instrument Mount allowed Up to three instruments to be mounted simultaneously at the Cassegrain focus and exchanged quickly. The Cassegrain focus instruments chosen for the observing campaign were NSFCAM, a 1- to 5- $\mu\text{m}$  camera and low-resolution spectrometer (2), and CSHELL, a 1- to 5- $\mu\text{m}$  high-resolution array spectrometer and imager (3), MIRAC2, a mid-infrared array camera (4), and IRSHELL, a mid-infrared high-resolution array spectrometer (5). MIRAC2 was commissioned on July 13 with a 128x128 Si:As detector array which was used between 2 and 21  $\mu\text{m}$ . A new 20 x 64 detector array in IRSHELL, used between 7 and 17  $\mu\text{m}$ , was first used on July 19. At Coude focus, the Goddard Infrared Heterodyne Spectrometer (IRHS) provided the highest spectral resolution in the 10 - 12  $\mu\text{m}$  spectral region ( $\lambda/\Delta\lambda \sim 10^6$ ), and measured individual spectral line shapes emitting from Jupiter's stratosphere (6).

## Fragments

One week before impact, fragments K, R and Q1 were slightly inside the nominal edge of the Jovian magnetosphere at some 70 Jovian radii from the center of Jupiter. At that time, no nuclei were detected above the noise limit at 1.25  $\mu\text{m}$  wavelength, even though the fragments had been detected at the IRTF in the preceding January and May at the same wavelength with a signal-to-noise ratio of a few hundred with a similar system sensitivity and noise. If most of the near-infrared light from the comet was contributed by scattering from the dust in the tail, then this result is consistent with the observations of Jewitt and Kalas of July 19 (unpub. comm. ), who found no

evidence of the dust tails for fragments P2, Q1, Q2, S, R, and W at 0.89  $\mu\text{m}$ . Possible mechanisms for this behavior are electrical charging of the dust in the Jovian magnetosphere, followed by dispersal due to the Lorentz force produced by crossing Jupiter's magnetic field or disruption of the dust particles due to electrostatic repulsion.

Fragment K was detected at  $2.26 \pm 0.03 \mu\text{m}$  with signal-to-noise ratio of 5-10 on July 19, when it was 150 to 60 arcmin (4.7 to 2.7 Jovian radii) from the center of the planet before impact. This wavelength minimized scattered light from Jupiter which dominates the sky background 10 arcmin away). The fragment appeared extended both along and perpendicular to the direction of orbital motion (Fig. 1). This was a surprising result, given the non-detection of the previous week (the signal at  $2.26 \mu\text{m}$  should be some 20 times less than at  $1.25 \mu\text{m}$ ) together with the increased noise and reduced sensitivity due to the scattered light from Jupiter. The increased flux may have been due to dust released in a new tidal breakup as the fragment approached the planet.

Preliminary analysis of observations made of Jupiter's ring at  $2.26 \mu\text{m}$  shows no change between May and August of 1994, ruling out any short-term input of dust to the rings or cometary dust - ring dust collisions. Continuing observations will determine the effect of the "dust wings" (11) of the comet train on the rings.

## Impacts

Fragments B and F. MIRAC2 detected no extraordinary phenomena near Jupiter's limb at the impact latitude for the B and F fragments, although data were acquired three standard deviations before and after the predicted impact times (10). MIRAC2 and NSFCAM detected signals associated with the C, G and R impacts at similar wavelengths, however (table 1). Both fragments B and F were displaced from the line formed by the brighter fragments in pre-impact comet images (11), and they were probably smaller in mass or their nuclei more prone to efficient tidal breakup just before entry.

Fragment C. On July 17, NSFCAM acquired images continuously from 6:53 to 7:44 UT with 3-4 sec time resolution using a narrow-band filter centered at  $2.248 \mu\text{m}$  with a bandpass of 1% to measure the C impact. During the first 21 minutes of this interval we imaged Io, Europa and the

predicted impact site simultaneously in an effort to detect Io's reflection of any impact emission. Io was well placed to reflect radiation from the impact site (500 from zenith at the impact site and 376,000 km distant, with impact-Io-Earth angle 760), but Europa was not (87° from zenith, 665,000 km distant, and with an impact-Europa-Earth angle of 1560). Accounting for surface albedo, a reflection from Io would have been some 100 times that from Europa, which served as an ideal brightness standard in each image. Figure 2 shows the changes in the brightness of Io, Europa, and the ratio of Io to Europa brightness during the satellite observing sequence. A spike of 6% amplitude occurs only in the Io and ratio data at 7:03:11 UT, but it involves only a single measurement, and a similar smaller spike occurs in the Europa brightness at 6:54:50 UT. The Io/Europa flux ratio also increases after 7:07 UT, but this is the result of a steady decrease in the brightness of Europa, not an increase in the brightness of Io. In summary, Io's and Europa's brightnesses were constant to  $\pm 1.5\%$  during this interval and show no convincing evidence of reflection of any impact radiation.

As NSFCAM continued to record images, the frame center was moved to Jupiter at 7:14:40 UT. At this time, a new feature was just becoming visible above Jupiter's limb. The A fragment impact site, just over one Jovian rotation old, was still bright in the foreground near the limb as the C impact radiation evolved in time. Figure 3 shows a small subset of images from this sequence. Figure 4 shows the lightcurve (the time variation of the flux) of the radiation as it grew and decayed between 7:15 and 7:45 UT. The lightcurve shows considerable structure on timescales of about 1 minute during its rise to maximum brightness at 7:23 UT, when it reached 80% of the brightness of Io. After an exponential drop, the signal reached a constant brightness of about 3% of the maximum that persisted until 7:33 UT.

**Fragment G.** For the NSFCAM G fragment impact observations on 18 July UT, we cycled between narrowband (2 - 5%) filters centered at 2.295  $\mu\text{m}$  and 4.78  $\mu\text{m}$ . Following the successful measurement of the C impact radiation at a single wavelength, we sought to measure subsequent impacts at two wavelengths to characterize the evolution of both temperature and solid angle for the emission source. We sought to differentiate between continuum emission from hot particles and possible line emission or reflected sunlight at 2.295  $\mu\text{m}$  by comparing with 4.79- $\mu\text{m}$  radiation where Jupiter's atmosphere is transparent and reflected sunlight is minimized. Heavy fog forced us to

close the dome until 7:35 UT when a temporary clearing allowed us to observe the G impact signal during its rise. At 7:44 UT, the 4.78- $\mu\text{m}$  signal became so bright that it saturated the detectors. At 8:09 UT the signal was lost in increasing fog which also required dome closure. Fig. 5 includes the last image through the 4.78- $\mu\text{m}$  bandpass prior to saturation. The bright emission at this wavelength suggests that continuum thermal emission comprised a major component of the signal.

**Fragment R.** On July 21 UT, MIRAC2 observed the impact of fragment R into Jupiter at three thermal infrared wavelengths: 7.85, 10.3, and 12.2  $\mu\text{m}$ , in sequential samples using a 2% circular variable filter an average of every 17 seconds. Continuous imaging of Jupiter in this mode began at 5:08 UT, and extended to 5:55 UT, after which measurements were made more often at 7.85  $\mu\text{m}$  than at the other wavelengths, constituting the data set for a seismic wave search. The first unambiguous evidence for excess infrared radiation from the impact appeared in a 7.85- $\mu\text{m}$  image taken at 5:40:57 UT. Figure 6 shows successive images just after this time. The emission reached a peak at each wavelength at approximately 5:44 UT. Figure 7 shows the amount of thermal radiation emitted at the impact location in excess of pre-impact values, after correcting for variations of sky emission. We stress that the provisional flux estimates shown are not sufficiently precise to compute useful color temperatures and angular sizes of the emitting region from these data, and we plan to report absolutely calibrated results at a later time. Excess fluxes are clearly sustained for at least 30 minutes after the initial detection, particularly at 10.3  $\mu\text{m}$ .

**Discussion.** Thermal emission, rather than reflected sunlight, is most likely the dominant source of the infrared flux. To match the peak brightness of the R signal at 10.3  $\mu\text{m}$ , a unit-albedo Lambert disk reflecting sunlight would require a radius larger than Jupiter. Because the C signal is 80% of the brightness of 10, a high-albedo satellite at 2.248  $\mu\text{m}$ , an optically thick cloud of high-albedo particles approximately 3000 km, the same size as 10, would be required to match the measured C fireball flux. The gross structure of the C and R lightcurves is similar despite the large wavelength difference, suggesting that the C impact signal is also thermal emission. If fragment C entered Jupiter's atmosphere at  $7:14 \pm 0.03$  UT as seen from the earth (12), then the time delay between entry and the observed peak emission was  $9 \pm 3$  min. If fragment R entered Jupiter's atmosphere at  $5:36 \pm 0.03$  UT (12), then the time delay between entry and observed peak emission

was  $10 \pm 3$  minutes. These delays are considerably longer than that calculated in several pre-impact numerical simulations of the events (13), which predicted delays of 100-200 sec between entry and appearance of a fireball or shock front above the limb. Plausible explanations include later impact times than current estimates, deeper penetration of the fragments or slower rise times of the heated gas than predicted, increasing opacity of the source with time, and atmospheric heating by the fallback of ejects.

### Atmospheric Temperatures

Several thermal infrared wavelengths dominated by the opacity of well-mixed  $\text{CH}_4$  and  $\text{H}_2$  gas were chosen to measure the temperature field, similar to a long time series of temperature measurements (14). One of the first signs of perturbations of the atmospheric temperatures by impacts was observed at  $7.85 \mu\text{m}$ , where strong  $\text{CH}_4 \nu_4$  fundamental band lines emit thermal radiation from  $\sim 10$  mbar total pressure. Figure 8 clearly shows the warming of the stratosphere by the E impact on July 18. This radiation might also be the result of thermal emission from particles lofted into the warm stratosphere, but no similar enhanced emission is seen at nearby  $8.57 \mu\text{m}$ , except for the G and L sites within 10 hours of their impacts. Therefore, it is much more likely that the enhanced enhanced thermal radiation at  $7.85 \mu\text{m}$  arises from warming of the stratosphere, rather than particulate emission, without invoking special spectral properties for the particles. The peak of the brightness temperature for the E site in Fig. 8 is some 1.5 Kelvins higher than its surroundings, and it is roughly 20,000 km in diameter. The Q1 and R impact sites were found to be 3 - 4 Kelvins warmer than their surroundings within 10 hours of their respective impacts. The large extent of these warm areas offers circumstantial evidence that warm particles and gases deposited by the descending impact ejects were responsible for their heating. On July 21, the E impact site had cooled to less than 0.5 Kelvin warmer than its surroundings, and barely above the noise level (Fig. 8). The L site, 2 Kelvins warmer than its surroundings on July 20, had cooled by  $\sim 1$  K 19 hours later. This cooling rate implies a characteristic time scale on the order of 2 days. This is consistent with the image taken of the same hemisphere on July 28, showing that the feature is no longer detectable. The radiative time scale in this part of the atmosphere is on the order of years (15), ruling out radiative cooling as the primary energy sink. We tentatively suggest



that temperatures are being restored to their **unperturbed** values **convectively**.

Another approach to measuring stratospheric temperatures assumed, on the basis of earlier studies (16,17), a constant ethane ( $\text{C}_2\text{H}_6$ ) mixing ratio of  $2.8 \times 10^{-6}$  above the **tropopause**, where emission lines were measured in order to determine significant changes in the stratospheric **temperature**. Days after the impacts, no significant temperature increase in the region of line formation **was** indicated, assuming simple temperature profiles (Fig. 9). However, **some** increase in the continuum emission was indicated, which is controlled **by** tropospheric temperatures.

Observations sensitive to tropospheric temperatures between 150 and 400 mbar pressure were made at 13.0, 17.2, 17.8 and 20.8  $\mu\text{m}$ , where the opacity of the atmosphere is dominated by the collision-induced opacity of molecular hydrogen. Figure 10 shows images of thermal emission at 17.2  $\mu\text{m}$ , sensitive to temperatures at the top of the troposphere near 150 mbar, and at 13.0  $\mu\text{m}$ , sensitive to temperatures near 400 mbar. The July 21 images show that the L impact significantly raised the temperature of the troposphere by at least 4 K at 150 mbar and 1.5 K at 400 mbar. The G impact site is identifiable on the 17.2- $\mu\text{m}$  image, and its temperature is some 2 K above the ambient temperature of the **region**. On the other hand, the the E impact site, observed on July 18 within 13 hours of impact, showed a barely discernible temperature increase. At subsequent times, Figure 10 shows that the 400-mbar temperature perturbation is **no longer** detectable above the noise and was probably convected away rapidly. However, the 150-mbar temperature perturbation of the I, impact site was **recognizable** above the noise as late as two weeks after the impact at roughly 1.5 - 2.5 K above the surrounding temperature, While this time scale is clearly longer than either the time scale for restoring the 10-mbar or the 400-mbar temperatures, it is still shorter than the radiative time scale, and convection is still likely to be the dominant mechanism restoring pre-impact temperatures.

#### Atmospheric Chemistry

$\text{NH}_3$ . in the observations which addressed a variety of possible changes of atmospheric chemistry, one of the most prominent discoveries **was** that of  $\text{NH}_3$  emission in Jupiter's stratosphere over impact sites. Figure 11 compares the thermal emission from Jupiter detected by IRSHELL near the impact latitude at the center of a strong  $\text{NH}_3$  feature with emission off the line center. The spectrum at

the peak of the emission from the K impact site is shown in Fig. 12. Fig. 11 clearly shows a strong morphological difference between the emission arising from the continuum, controlled by the temperature field and by  $\text{NH}_3$  absorption near 3(10 mbar) pressure, and the emission arising from the center of a strong  $\text{NH}_3$  spectral line near 50. ] 00 mbar total pressure. Fig. 12 illustrates that the spectrum of a nearby off-impact region can be modeled by the same temperature structure as fitted this region in 1989 (18) and a  $\text{NH}_3$  mixing ratio equivalent to 40% of the  $\text{NH}_3$  saturated vapor pressure up through the temperature minimum. Above the ~100-mbar temperature minimum level, however, the  $\text{NH}_3$  mixing ratio cannot exceed  $2 \times 10^{-6}$ , the consequence of photochemical destruction in the stratosphere. At the fragment K impact site, the  $\text{NH}_3$  emission feature in Fig. CH2 is matched by raising the  $\text{NH}_3$  stratospheric mixing ratio to  $8 \times 10^{-8}$ . This value is close to that of the fully saturated mixing ratio at a temperature minimum near 111 K, nearly the same as the pre-impact temperature minimum. However, the radiance at the cusp between the  $\text{NH}_3$  absorption and emission is matched only by raising the value of the minimum temperature to 118 K. This difference is higher than that implied by the brightness temperature difference in those MIRAC2 data discussed above, but the  $\text{NH}_3$  emissions should be more sensitive to local temperature variations. It is a narrower vertical probe than the  $\text{H}_2$  emission sensed by MIRAC2, as a consequence of the rapid vertical falloff of the  $\text{NH}_3$  abundance. The other emission line shown in Fig. 12 at  $907.74 \text{ cm}^{-1}$  is of unknown origin but is definitely not  $^{15}\text{NH}_3$ ,  $\text{PH}_3$ , or  $\text{C}_2\text{H}_6$ . Another IRSHELL observation near  $948 \text{ cm}^{-1}$ , taken shortly after the one shown in Figs. 11 and 12 shows tentative evidence for enhanced  $\text{C}_2\text{H}_4$  emission distributed uniformly in the stratosphere with a mixing ratio of 3 ppb.

The IRHS also observed ammonia injected into the stratosphere at the Q1 impact site, measuring a strong line at  $892.1577 \text{ cm}^{-1}$  (Fig. 13). Using the temperature profiles constrained by the IRHS measurements of  $\text{C}_2\text{H}_6$ , the data can be fit by a uniform stratospheric  $\text{NH}_3$  mixing ratio of  $1 \times 10^{-8}$ . If the stratospheric temperature profile were 10 Kelvins warmer, the corresponding  $\text{NH}_3$  mole fraction fitting the data would be about a factor of 5 lower. These abundances are well below the saturation level for stratospheric temperatures, and measurements of the line shape and width show that the line emission originated in the 1- to 30-mbar pressure regime. Figure 9 shows the

contribution function near line center. It indicates that the impact-distributed  $\text{NH}_3$  gas at least as high as the 1-mbar pressure level. Measurements centered  $8^\circ$  in longitude away from the Q1 impact site yielded an upper limit of  $2 \times 10^{-9}$  for the  $\text{NH}_3$  mole fraction (Fig. 9b). The precision of these values is on the order of 30%.

Increased  $\text{NH}_3$  emission over nearly every impact site was also detected in the much broader spectral bandwidth observations by MIRAC2 at 10.74  $\mu\text{m}$ . The decay of this emission in time between July 17 and Aug. 6 is consistent with the rate of photochemical destruction expected for the  $\sim 10$ -mbar level. By photolysis alone the  $\text{NH}_3$  abundance should be reduced by a factor of at least 6 in about a week, where the precision of these values is on the order of 30%.

PH<sub>3</sub>. Figure 14 shows a CSHELL spectrum which is sensitive to the total amount of  $\text{NH}_3$  and  $\text{PH}_3$  gas overlying the atmosphere in the 1 - 5 bar pressure regime. Prominent features in the spectra include a Jovian  $\text{NH}_3$  line at  $1971.2 \text{ cm}^{-1}$  and the  $\nu_2 + \nu_4$  Q-branch of  $\text{PH}_3$  at  $1972.2 \text{ cm}^{-1}$ . A weaker Jovian  $\text{NH}_3$  line is blended with the high-frequency shoulder of the  $\text{PH}_3$  Q branch. There is a noticeable difference in the strength of the  $\text{PH}_3$  Q branch with all three spectra taken at impact latitudes showing a significantly weaker absorption feature. This could be the result of either a reduced column abundance of  $\text{PH}_3$  or of emission in the  $\text{PH}_3$  Q-branch from warm gas partially filling in the absorption feature. In contrast, the  $\text{NH}_3$  feature appears to be approximately constant between north and south.

CO. Figure 15 shows another CSHELL spectrum with a weak CO line which is most probably the result of narrow CO emission filling in the center of the broader CO absorption line. The presence of CO emission 10 days after the impacts implies that it must be relatively high in the stratosphere, at 10-5 bar or less, where the temperature might be warm enough ( $T \geq 280\text{K}$ ) to produce observable emission if CO were enhanced at the impact sites (19). Oxygen is a normally a rare element in Jupiter's upper troposphere and stratosphere, where its reservoir of oxygen is  $\text{CO}$  which is most likely distributed with a uniform mixing ratio of 1ppb throughout the pre-impact stratosphere. The impact of even a modest ( $10^{15} \text{ g}$ ) comet would have increased this small amount of CO substantially, both directly from CO in the comet itself and indirectly from any other oxygen containing material which eventually is converted to CO. This observation provides

some evidence that the impacts provided some small stratospheric enhancement of the ordinarily stable CO molecule.

Other gases. The presence of  $H_2O$  lines near  $11\mu m$  was searched for with IRHS, and the presence of  $H_2S$  near  $8\mu m$  and  $HCN$  near  $13\mu m$  was searched for with IRSHELL in a number of impact regions at different times after impact, although generally never less than one day after impact.  $H_2O$  and  $H_2S$  might have abundances enhanced at impact sites by upwelling of tropospheric gas, and  $HCN$  might have been created as a result of impact shock chemistry. None of these were detected, but further analysis will be required to retrieve upper limits.

#### Atmospheric Particulate

Our investigation of the atmospheric particulate used both reflected near-infrared sunlight between 1 and  $4\mu m$  and thermal emission between  $4.6$  and  $8.57\mu m$ , using NSFCAM Up to  $5.3\mu m$  and MIRAC2 from  $5\mu m$  and longer wavelengths. Here we report some of the preliminary NSFCAM results. Figure 16 shows 4 of the 17 wavelengths sampled by NSFCAM to investigate atmospheric particulates and aurora. These near-infrared images showed particulates prominently at most of the impact sites, including images in strong  $3.4\mu m$   $CH_4$  absorption, sensitive to sunlight reflected from particles at the pressure level of 3 mbar or less. Prior to the impacts, no reflection from atmospheric particulate was ever seen at this wavelength, but emission from  $H_3^+$  aurorae near the poles and a faint auroral glow over the rest of the planet were detectable. Gaseous absorption is weaker at  $2.27\mu m$ , but still strong enough to absorb all sunlight except that reflected from particles in a stratospheric haze layer at pressures less than 100 mbar. At  $2.10\mu m$ , it is weaker still and absorbs all sunlight except that is reflected from a tropospheric  $NH_3$  ice cloud near 600 mbar and the stratospheric haze layer. Impact sites K, 11, Q 1, G, R, and L are many times brighter than the normal planetary features at these wavelengths, such as the polar hazes and the Great Red Spot. This indicates that particulate resulting from the impacts are present in the upper stratosphere at pressures less than several millibars. On the other hand, there is no sign of the impact sites in the  $1.60\mu m$  images which are sensitive to the deepest cloud reflectivities. From this we deduce that the difference in absorption optical depth between the impact-related particles and those in the rest of the atmosphere is quite low in the near infrared, in contrast to the visible and near ultraviolet

(12).

We examined the H and the bright G, L, and Q1 impact sites observed between July 21 and August 7. The latitudinal and longitudinal extents of the isolated Q1 feature did not change more than 10%. Also during this period, the core brightnesses of the G, I, and Q1 features did not change more than our 10% level of uncertainty, but the brightness of the H feature dimmed by 20%. An aerosol model structure consisting of bright 0.25- $\mu\text{m}$  particles distributed uniformly in altitude between 200 mbar and 1 mbar is consistent with the observed impact site brightnesses seen in the infrared by the IRTF and in the visible by the Hubble Space Telescope (20). In the core of the G feature, the model indicates particle column densities of  $3.0 \pm 0.5 \times 10^8 \text{ cm}^{-2}$  corresponding to opacities of  $2.4 \pm 0.4$  at  $0.89 \mu\text{m}$  and  $0.085 \pm 0.015$  at  $2.14 \mu\text{m}$ . The Q1 and R impact sites are 30% and 50% dimmer than the G impact site at  $2.14 \mu\text{m}$ , implying their aerosol burden is proportionately smaller.

Figure 17 shows the evolution of the K feature. On July 28, the particulate at the fragment K impact site formed an elliptical spot spanning roughly  $38''$  of longitude and  $17^\circ$  of latitude, centered at  $\sim 45^\circ\text{S}$  and  $278^\circ\text{W}$  longitude (in System 111 the longitude associated with the magnetic field). By August 7, the feature had evolved to an extended but roughly symmetrical spot measuring  $44^\circ$  longitude at its widest points and about  $16^\circ$  of latitude. The feature seems to have spread out zonally at a latitude of  $45^\circ\text{S}$ . The evolution of K indicates a zonal (east-west) expansion speed of about  $6.14 \pm 1.54 \text{ m/sec}$  ( $3.07 \pm 0.77$ ). This implies zonal wind speeds which are much slower than in the underlying troposphere,  $8.0 \text{ m/sec}$  retrograde at  $45.3^\circ\text{S}$  (21), indicating a negative zonal velocity gradient with altitude (a decreasing vertical shear velocity). This confirms the prediction from the thermal wind equation applied to Voyager infrared data (22).

## Aurora

The collision of Comet Shoemaker Levy 9 with Jupiter had a profound effect on its infrared  $\text{H}_3^+$  auroral emissions, which have been used to probe the Jovian aurorae and ionosphere since its first detection there (23). Formed indirectly from the ionization of  $\text{H}_2$  by impacting electrons, it is a sensitive tracer of energy deposition in the upper Jovian atmosphere. A number of studies using imaging at  $\sim 2\%$  spectral resolution at  $\text{H}_3^+$ -sensitive wavelengths at  $3.4$  and  $3.5 \mu\text{m}$  have shown

the extent and variability of the auroral emissions (24) and the exact field lines onto which they map (25). The emission of the northern and southern aurora are generally similar, with the south being slightly brighter. This was the situation as measured prior to the impacts on July 12. The northern auroral zone measured at  $3.4\ \mu\text{m}$  had an intensity of  $1.3 \times 10^{-12}\ \text{W/m}^2/\mu\text{m}$ , compared with the southern aurora at  $0.8 \times 10^{-12}\ \text{W/m}^2/\mu\text{m}$ . Images taken on July 17, about an hour after the impact of Fragment C, were similar.

However, by July 27, the next available measurement opportunity, the northern auroral zone appeared very much brighter than the south (Fig. 16). The northern emission had increased by a factor of nearly four to  $4.7 \times 10^{-12}\ \text{W/m}^2/\mu\text{m}$ , and the southern aurora was slightly dimmer than it was prior to impact. Thus, at its peak, the northern emission was 6-7 times brighter than the southern emission. Over the following ten days, the relative and absolute intensities returned to a more normal state. By August 7, the ratio of northern to southern emissions varied between 0.5 and 4, depending on the central meridian longitude of the image.

Other auroral-related infrared phenomena, are the polar stratospheric hot spots, which are powered by thermalization of high-energy charged particles cascading down magnetic field lines (26, 27). Before the impact, the north polar hot spot was located quite consistently at  $60^\circ\ \text{N}$ ,  $180^\circ\ \text{W}$  in System 111 (27), but it was not detected during the impacts. It was detected again on July 28, missing on Aug. 4 and 5, and it returned on Aug. 6 (Fig. 8). Presuming that the dust environment associated with SL9 fragments were responsible for short-term modulations of the electromagnetic environment, we tentatively conclude that the time scales associated with the generation of this phenomenon are short. We intend to search the existing data set for  $7.8\text{-}\mu\text{m}$  images of the north polar region in the months before the impact epoch to assess the likelihood that this phenomenon is unrelated to the entry of Comet Shoemaker-Levy 9 in the Jovian system.

#### Remaining Work

Much remains to be done. The ongoing search for evidence of impact-related atmospheric waves may provide a unique probe of the structure and dynamics of the deep atmosphere. Near-infrared colors and dust dynamics will also be modeled to determine whether water ice was detected, adding considerable evidence as to whether SL9 was a comet or an asteroid. Accurate photometric (28) and

geometric calibration, and intercomparison of the atmospheric experiment results will provide the strongest possible constraints on atmospheric properties, even for regions of the planet not affected by the impacts. Collaborations with other observers will also fill in spectral, spatial and temporal gaps in coverage. These data will be used to refine models of the Jovian system, particularly the atmosphere, and will be used to support the interpretation of observations made by Galileo mission. Within a few months, we hope to have a fully calibrated data set available as part of a national treasure of information on a very unique epoch in Jupiter's history and an exciting period in our personal and professional lives.

TABLE 1. SUMMARY OF IMPACT- RELATED OBSERVATIONS

Fragment	Instrument	Wavelength (s) (Pm)	Weather	Results/Comments
B	MIRAC2	7.85	Clear	No obvious effect
c	NSFCAM	2.248	Clear	Detailed time sequence, satellite photometry
F	MIRAC2	7.85	Some clouds	No obvious effect
G	NSFCAM	2.30, 4.78	Some fog and clouds	Some data, detector saturation
R	MIRAC2	7.85,10.3,12.2	Partly cloudy	Detailed time sequence
v	CSHELL		Cloudy	No data
W	NSFCAM		Cloudy	No data



## References and Notes

1. Science Team members are: A'Hearn, Baines, Deming, Dowling, Griffith, Goguen, Hammel, Hoffmann, Hunten, Jewitt, Kostiuk, Nell, Orton (Chair), and Zahnle.
2. J. Rayner, M. Shure, D.W. Toomey, I. Onaka, A. Denault, W. Stahlberger, D. Watanabe, K. Criez, I. Robertson, D. Cook and M. Kidger *Proc. SPIE* 1946, 490 (1993).
3. T. Greene, A. T. Tokunaga, D. W. Toomey, and J. S. Carr *Proc. SPIE* 1946, 313 (1993). Both NSFCAM and CSHELL are IRTF facility instruments and used new 256x256 detector arrays.
4. W. F. Hoffmann, G. G. Fazio, K. Shivanandan, J. L. Hera, L. K. Deutsch *Proc. SPIE* 1946, 449 (1993); W. F. Hoffmann, G. G. Fazio, K. Shivanandan, J. L. Hera, L. K. Deutsch. *Infrared Physics Technol.* 35, 175 (1994). MIRAC2 was constructed and is operated by Steward Observatory, University of Arizona, and the Smithsonian Astrophysical Observatory.
5. J. Lacy, J. M. Achtermann, D. E. Bruce, D. F. Lester, J. F. Ahrens, M. C. Peck and S. D. Gaalema *Publ. Astron. Soc. Pacific* 101, 1166 (1989). CSHELL is operated by the University of Texas at Austin.
6. T. Kostiuk and M. J. Mumma. *Appl. Opt.* 22, 2644 (1983); T. Kostiuk. *Infrared Phys. Techn.* 35, 243 (1994). Both the IRHS technique and its application to planetary atmospheric studies is also described in these papers.
7. M. Marley *Astrophys. J. Lett.* 427, L63 (1994); D. H. Hunten, W. F. Hoffmann, and A. I. Sprague *Geophys. Res. Lett.* 1, 1091 (1994).
8. J. Barrington, R. P. LeBeau, K. A. Backes, and T. E. Dowling *Nature* 368, 525 (1994).
9. Observations of fragments G and R within a few hours of impact were cut short due to inclement weather.
10. An unpublished communication circulated on electronic mail by P. Chodas, Jet Propulsion Laboratory, 4800 Oak Grove Dr., Pasadena, CA 91109, provided predicted times of

2:54:13±4:06 (1  $\sigma$ ) for B and 7:02:14±3:42 for C on July 17, 00:29:21±4:00 for F and 7:28:32±3:06 for G on July 18, and 5:25:56±4:36 UT for R on July 21.

11. H. Weaver *et al. Science* 203787 (1993).
12. H. B. Hammel, R. F. Beebe, A. P. Ingersoll, G. S. Orton, J. T. Clarke, J. R. Mills, A. A. Simon, R. A. West, E. De Jong, 'I'. E. Dowling, J. Barrington, L. F. Huber, E. Karkoschka, D. M. Kuehn, and A. Toigo. *Science*, Submitted.
13. T. J. Ahrens, T. Takata, J. D. O'Keefe, and G. S. Orton. *Geophys. Res. Lett.* 21, 1087 (1994); M. B. Boslough, D. A. Crawford, A. C. Robinson, and 'J'. G. Trucano *Geophys. Res. Lett.* 21, 1555 (1994); M. B. Boslough, D. A. Crawford, A. C. Robinson, and T. G. Trucano, *T.G. EOS* 75, 305 (1994); D. A. Crawford, M. B. Boslough, q'. G. Trucano, T. G., and A. C. Robinson *Shock Waves* 4, 47 (1994); T. Takat a, T. J. Ahrens, J. D. O 'Keefe, and G. S. Orton. *Icarus* 109,3 (1994); K. Zahnle and M.-M. Mac Low *Icarus* 108, 1 (1994).
14. G. S. Orton, *et al. Science* 252,537 (1991); G. S. Orton, *et al. Science* 265, 625 (1994).
15. M. Flasar. In Time-Variable Phenomena in the Jovian System (M. Belton, G. Hunt, R. West, eds. ), NASA Special Publication 494, 324 (1986).
16. T. Kostiuk, F. Espenak, M. J. Mumma, D. Deming, and D. Zipoy *Icarus* 72, 394 (1987).
17. I. Livengood, T. Kostiuk, F. Espenak, and J. Goldstein *J. Geophys. Res.* 9818813 (1993).
18. G. Orton, J. Iacy, A. Castillo, J. Achtermann, and P. Parmar. *Bull. Amer. Astron. See.* 24, 1041 (1992).
19. The temperature near 1  $\mu$ bar was derived as 200±50 K from the Voyager-2 UVS  $\alpha$  Leo occultation experiment, described by S. K. Atreya, T. Donahue, and M. C. Festou. *Astrophys. J.* 747, 1,43 (1981) and by M. C. Festou, S, K. Atreya, T, M. Donahue, B. R. Sandel, D. E. Shemansky, and A. I. Broadfoot. *J. Geophys. Res.* 86, 5715 (1981).
20. R. West, E. Karkoschka, A. J. Friedson, M, Seymour, K. H. Baines, and H. B. Hammel *Science*. Submitted.

21. S. Limaye *Icarus* 65,335 (1986).
22. P. J. Gierasch, B. J. Conrath, and J. A. Magalhaes. *Icarus* 67,456 (1986).
- 23 P. Drossart, J.-P. Maillard, J. Caldwell, S. J. Kim, J. K. G. Watson, W. A. Majewski, J. Tennyson, S. Miller, S.K. Atreya, J. T. Clarke, J. H. Waite Jr. and R. Wagener, *Nature* 340, 539 (1989).
- 24 R. Baron, R. D. Joseph, T. Owen, J. Tennyson, S. Miller and G. F. Ballester, *Nature*, 353, 539 (1991); S. J. Kim, P. Drossart, J. Caldwell, J.-P. Maillard, T. Herbst and M. Shure, *Nature*, 353,536 (1991).
- 25 R. Baron, T. Owen, J. Connerney, J. Barrington and T. Satoh, *Bull. Am. Astron. Soc.* 24, 1031 (1992).
- 26 S. J. Kim. *Icarus* 1'73,399 (1988).
- 27 J. Caldwell, A. T. Tokunaga and G. S. Orton. *Icarus* 53, 133 (1983).
- 28 The IRSHELL and IRHS data derive absolute radiance calibration by reference to a radiance source as a part of their first-order reduction. Certain CSH ELI. data will also be useful without absolute radiance calibration.
29. We thank the engineering staff of the Infrared Telescope Facility, headed by Paul Jensen, for their unstinting support in making so many late improvements to the telescope performance possible, This research was sponsored by various grants from the National Aeronautics and Space Administration and the National Science Foundation for work performed at each of the institutions with which the several authors of this paper are associated. The MIRAC2 upgrade to the 128x128 array was also supported by Steward Observatory, University of Arizona and Smithsonian Astrophysical Observatory. '1'. Livengood was a National Research Council Resident Research Associate. A'Hearn, Baines, Dayal, Deutsch, Espenak, Esterle, Fast, Friedson, Goguen, Griffith, Hammel, Harrington, Hoffmann, Hora, Huntten, Kelly, Knacke, Kostiuik, Lacy, Lisse, Miller, Nell, Orton, Sprague, Wells, Yanamandra-Fisher, Zahnle, and Zipoy were visiting astronomers at the Infrared Telescope Facility which is operated by the

University of Hawaii under contract to the National Aeronautics and Space Administration. We thank Research Systems, Inc. for donating several licenses for the Interactive Data Language (IDL) which was used to generate most of the graphics in this paper. B. Taylor is gratefully acknowledged for data reduction support.

## Figure Captions

Figure 1. Tentative image of fragment K (enclosed in circle), based on the average of 6 exposures from early in the imaging sequence of July 19. False colors have been used to enhance the faint signal from the fragment. The sequence of images were taken from 150 to 60 minutes before impact at  $2.36\ \mu\text{m}$  wavelength. Jupiter is just outside the field of view at the top of the frame, but the scattered light from Jupiter extends from the edge of the field all the way to the middle. The short, bright, diagonal streak near the end of the scattered Jovian light is a star, which made a trail while the fragment was tracked. A much fainter star trail can be seen merging into the scattered Jovian light near the edge of the frame.

Figure 2. Lightcurves for the satellites 10 (J 1) and Europa (J2) at  $2.248\ \mu\text{m}$  in the satellite reflected impact flash experiment observed by NSFCAM on July 17, 1994. The curves are all ratioed to their mean values in this time interval, and the J2 and J 1 /J2 ratios are displaced downward by 0.1 and 0.2, respectively, for clarity. Vertical arrows indicate times when the telescope was guided.

Figure 3. Images of Jupiter at  $2.248\ \mu\text{m}$  wavelength taken with NSFCAM on July 17, 1994 (UT). Times are displayed to the nearest minute in UT. The north and south polar hazes are visible in each image, as is the particulate feature associated with the impact of fragment A. By 7:40 UT, the C fragment has nearly assumed its asymptotic appearance as a particulate feature merely reflecting sunlight from the atmosphere similar to and slightly fainter than the A fragment particulate feature.

Figure 4. Lightcurve for the C fragment impact fireball observed with NSFCAM at a wavelength of  $2.248\ \mu\text{m}$  (see Fig. 3). The flux is normalized to its peak value.

Figure 5. Images of the G fragment impact fireball taken with NSFCAM in a filter at  $4.78 \pm 0.11\ \mu\text{m}$  (known as the narrow-band M filter) on 1994 July 18 (UT). Only the southwestern limb of Jupiter is visible. The dramatic increase in the plume brightness is evident in these images.

Figure 6. Images of the R fragment impact fireball taken with MIRA C2 on 1994 July 21 in three filters, centered on 7:42 UT. The observations were taken sequentially with 20-sec time

separations, starting with  $7.85\ \mu\text{m}$  (left),  $10.30\ \mu\text{m}$  (center) and  $12.20\ \mu\text{m}$  (right). The images are stretched logarithmically, in order to see Jupiter and the impact-related brightening at the same time.

Figure 7. Excess thermal emission generated by the impact of fragment R at wavelengths of 7.85, 10.3 and 12.2  $\mu\text{m}$ . The individual values were calculated by summing measured pixel intensities over a 4.2- by 4.2-arcsecond square centered on the impact site and subtracting an average of similar intensities obtained before 5:40 UT. Absolute calibration of the data has not been completed; fluxes have been scaled to the peak value. Provisional estimates for the peak excess fluxes are  $7 \times 10^{-8}$ ,  $4 \times 10^{-8}$ , and  $2 \times 10^{-8}\ \text{erg cm}^{-2}\ \text{sec}^{-1}\ \mu\text{m}^{-1}$  at 7.85, 10.3, and 12.2  $\mu\text{m}$ , respectively, integrated over the 2% filter emission in each image. After 5:55 UT the sky emission became highly variable in time and over the field of view of the camera. The error bars represent one standard deviation of background sky emission in each image. Larger systematic errors occur where the background sky emission varied substantially across a single image, making the correct amount of background to be subtracted uncertain.

Figure 8. Images of Jupiter's thermal emission at 7.85  $\mu\text{m}$ . The images, identified by the UT date and System-III longitude of the central meridian, were chosen to present nearly the same earth-facing hemisphere to show the evolution of stratospheric temperatures at several impact sites over time.

Figure 9. The nominal (non-impact) thermal profile used in the fit of the IRHS data, the resultant  $\text{NH}_3$  mole fraction profiles, and the contribution function corresponding to the center of the  $\text{NH}_3$  line.

Figure 10. images of Jupiter's thermal emission at 17.8  $\mu\text{m}$  (left) and 13.0  $\mu\text{m}$  (right), used to sound the 150-mbar and 400-mbar levels, respectively. The images, identified by the UT date and System-1 longitude of the central meridian, were chosen to present nearly the same earth-facing hemisphere to show the evolution of tropospheric temperatures at several impact sites over time.

Figure 11. IRSHELL spectral images of the impact latitudes. The images were created by scanning over the impact sites north and south by 6 arcsec with the 20-arcsec slit oriented

parallel to the equator. The two panels are images taken from different portions of the spectrum simultaneously. The upper image was derived from the center of the  $V_2P_13$  line of  $NH_3$  at  $908\text{ cm}^{-1}$ ; the lower image was derived by averaging the radiance off the line center. Contours on the upper image are shown between radiances of 0.00 and 0.45, and on the lower image between 0.00 to 0.18 at intervals of  $0.20\text{ erg sec}^{-1}\text{ cm}^{-2}\text{ ster}^{-1}(\text{cm}^{-1})^{-1}$ . The strong emission arises from impact site K.

Figure 12. IRSHELL spectra at (upper curves) and 6 arcsec away (lower curves) from the K impact site. This is another portion of the data set shown in Fig. 11. Observations are shown in solid and models in dashed curves. The absorption feature at  $908.95\text{ cm}^{-1}$  is due to absorption in the earth's atmosphere.

Figure 13. (a) Ammonia emission line from the stratosphere of Jupiter at the site of the impact of fragment QJ 8.5 days after impact. Measurements were made at  $0.00083\text{ cm}^{-1}$  spectral resolution. Spectrum has been smoothed and presented at  $0.00166\text{ cm}^{-1}$  effective resolution. The solid curve represents the best fit for a temperature profile off the impact site. (b) The same spectral region measured  $8^\circ$  off the QJ impact site.

Figure 14. Spectra of Jupiter made with CSHELL on 1994 August 1. The wavelength scale is approximate, with the nominal dispersion of the CSHELL used and the zero point set by the strong  $PH_3$  feature in Jupiter. The flux scale is arbitrary. The smoothed spectrum of  $\alpha$  Virginis at the top of the figure shows that only weak terrestrial lines occupy this wavelength interval. Five separate spectra are shown; three were obtained near the impact latitudes in the south. The first (dashed line) was our best attempt to line up with the spots that were easily visible at 2 pm. The second (dotted) was 1 arcsec north, the third (dash-dotted), one arcsec south of the optimal position. A fourth spectrum (solid) was recorded at the conjugate northern latitude of the first spectrum, approximately  $45^\circ$  N. A 10% slope was removed from two of the four spectra. The spectral feature at  $1970.4\text{ cm}^{-1}$  is a terrestrial  $H_2O$  line.

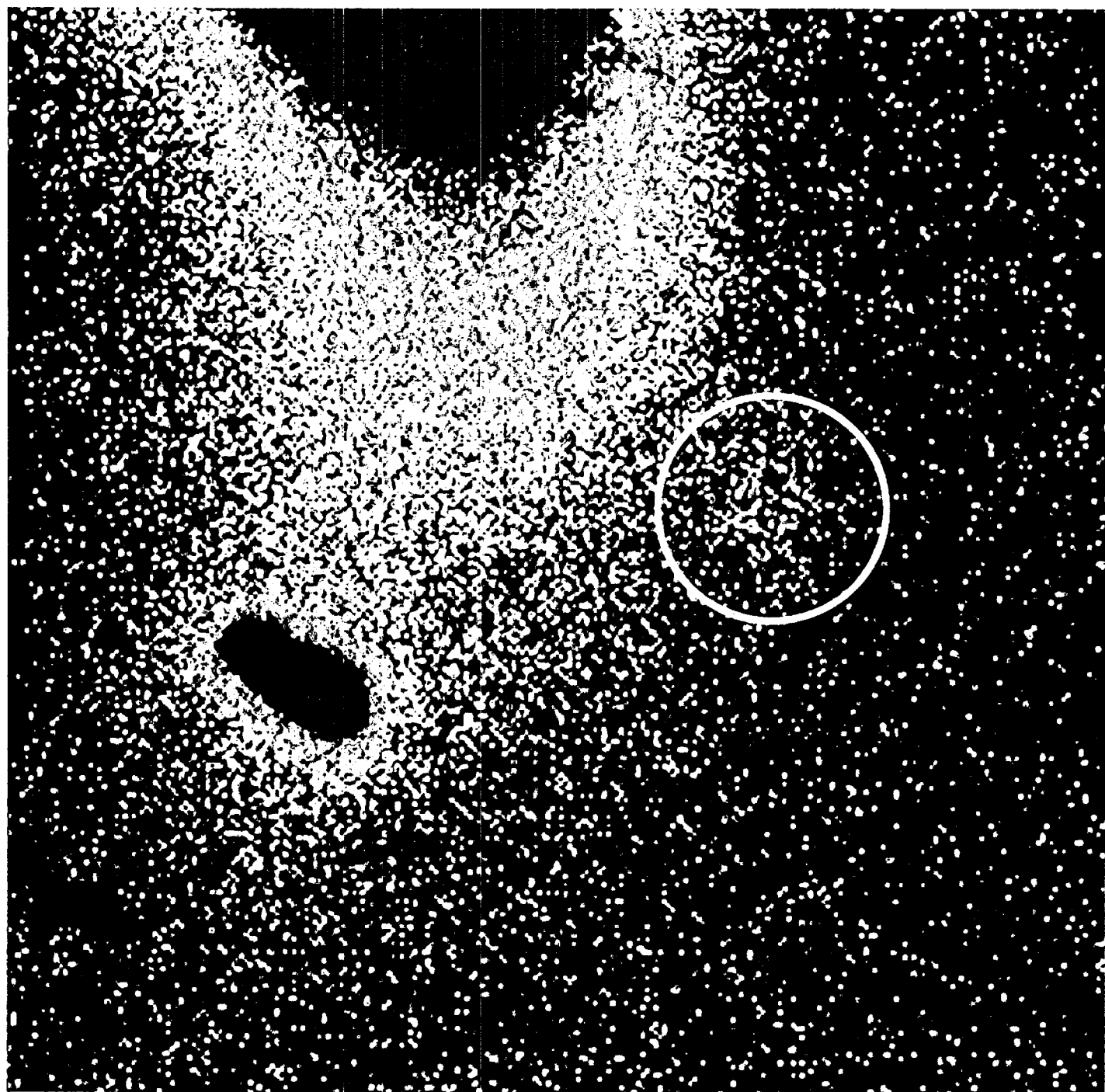
Figure 15. Spectra of Jupiter made with CSHELL on 1994 August 2. As with the preceding figure, the wavelength scale is approximate and the flux scale is arbitrary. The solid line shows a spectrum near the CO 1-O R5 line with the slit centered along the impact latitude at

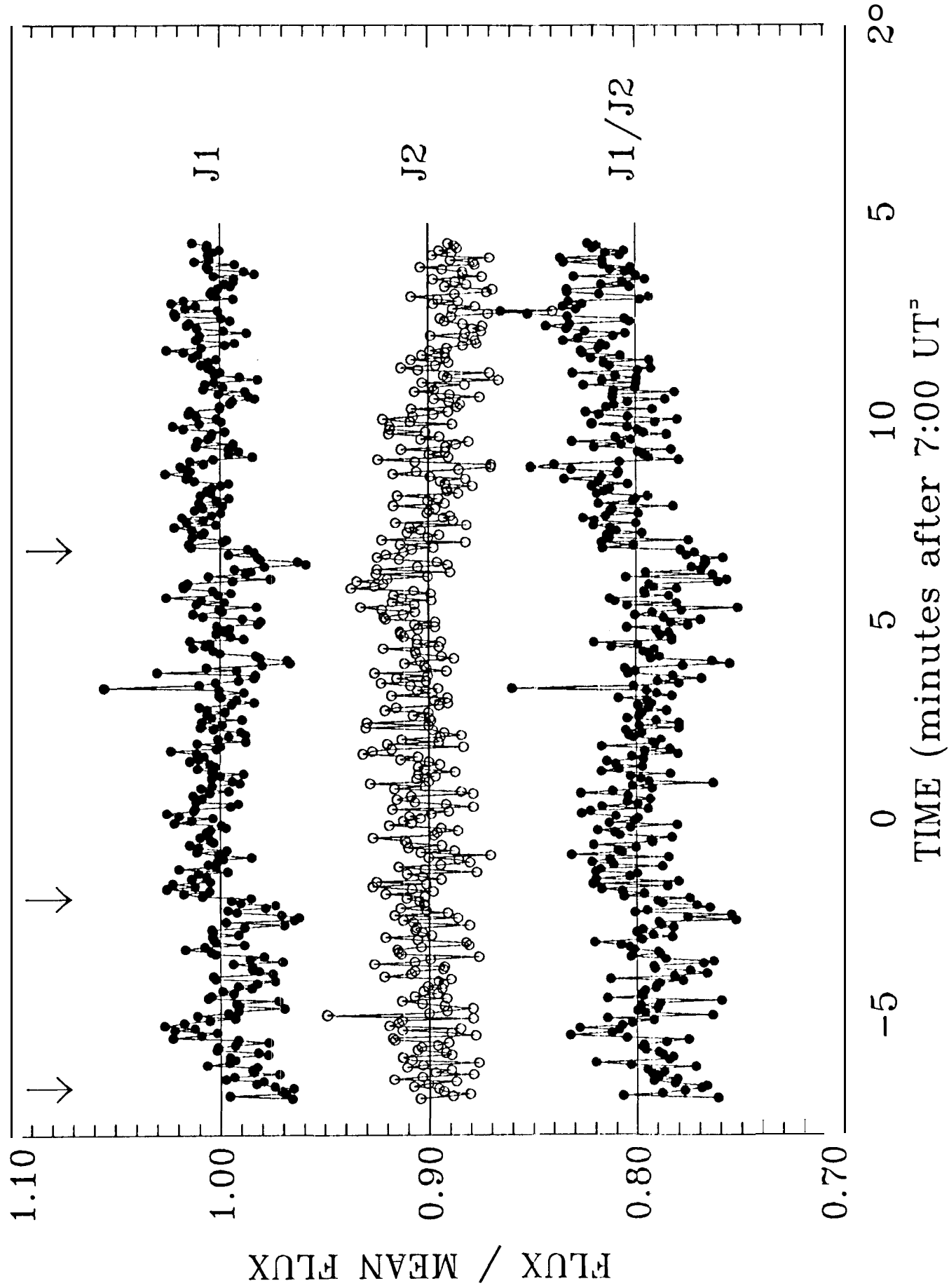
45°S, and the dashed-dotted curve shows a spectrum taken at 45°N. The dotted curve shows the ratio of the two spectra scaled upward by a factor of 1000,

Figure 16. Images of Jupiter using NSFCAM taken on July 27, 1994. The images are logarithmically stretched to show the greatest dynamic range. The images were taken near 8:28 UT when the central meridian is 228°W in System J1. In these sequence of figures, the atmospheric gaseous absorption increases monotonically with wavelength. Only the highest particulate reflect sunlight, in the 3.41  $\mu\text{m}$  image which is otherwise dominated by  $\text{H}_3^+$  aurora at the poles and a faint airglow over the planet as a whole.

Figure 17. A sequence of images of Jupiter using NSFCAM at 2.27  $\mu\text{m}$  showing the evolution of the K fragment impact site particulate feature. All images are logarithmically stretched.







7:15



7:21

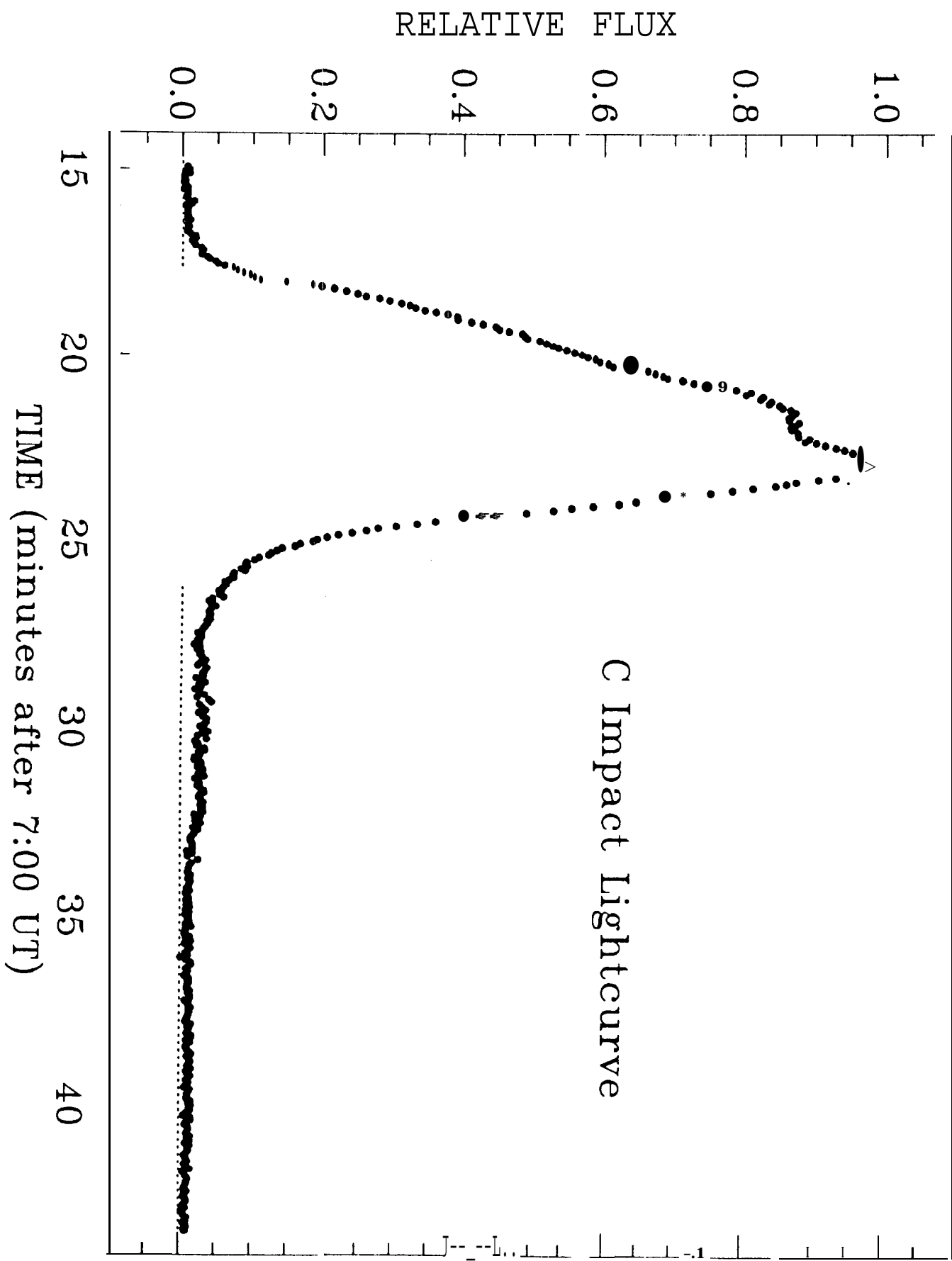


7:27



7:34







7:39:45 UT



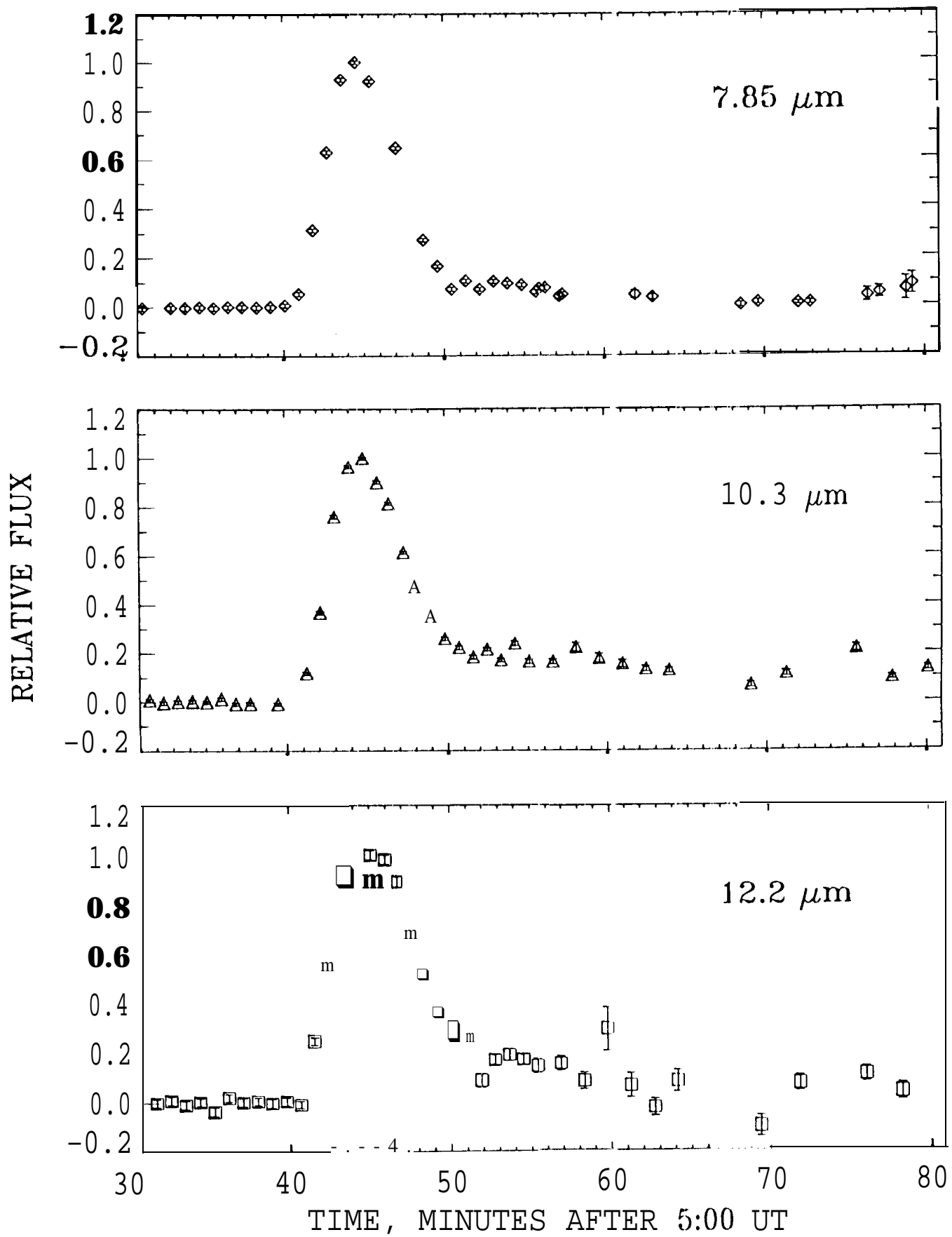
7:41:41 UT

7.85  $\mu\text{m}$

10.30  $\mu\text{m}$

12.20  $\mu\text{m}$





1994 Jul 18  
146° W



1994 Jul 21  
185° W



1994 Jul 28  
173° W



C + 21h  
A + 32h  
E + 13h

1994 Aug 4  
189° W



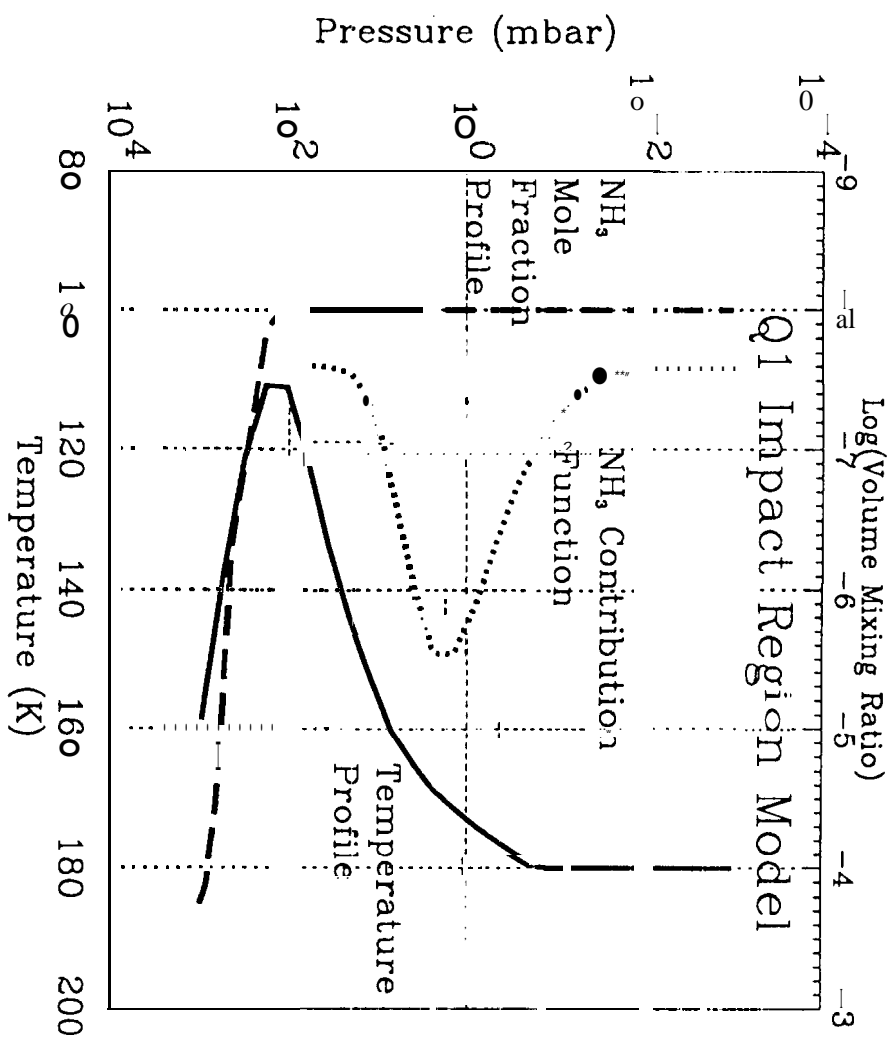
1994 Aug 5  
223° W



1994 Aug 6  
181° W







1994 Jul 20  
342° W



G + 42h ——— ↑  
L + 3h ——— ↑

1994 Jul 21  
350° W



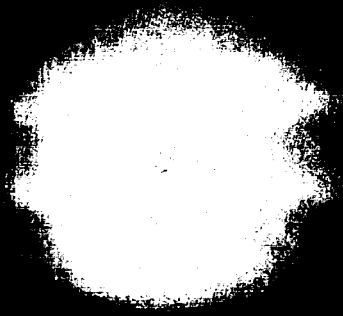
↑ K + 15h      R + 1h ——— ↑  
                                 L + 44h ——— ↑      ↑ K + 32h

1994 Jul 28  
252° W



L ——— ↑  
                 ↑  
K ——— ↑

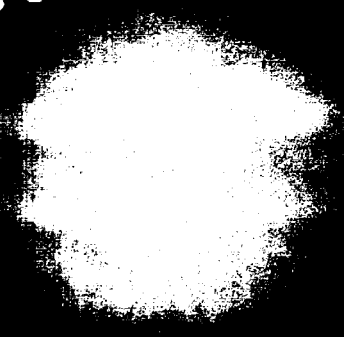
1994 Jul 28  
250° W

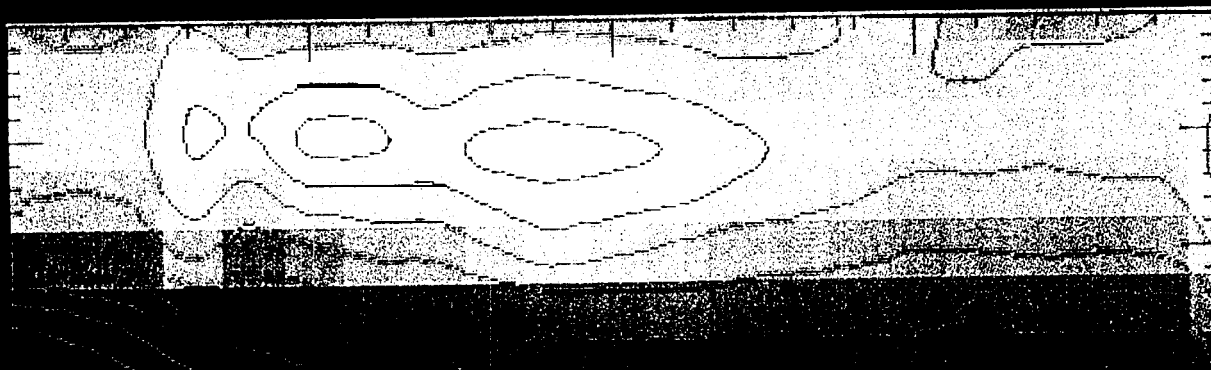
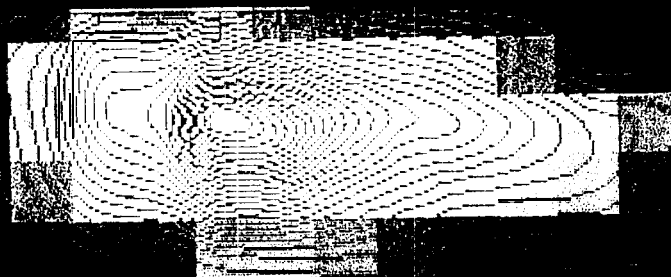


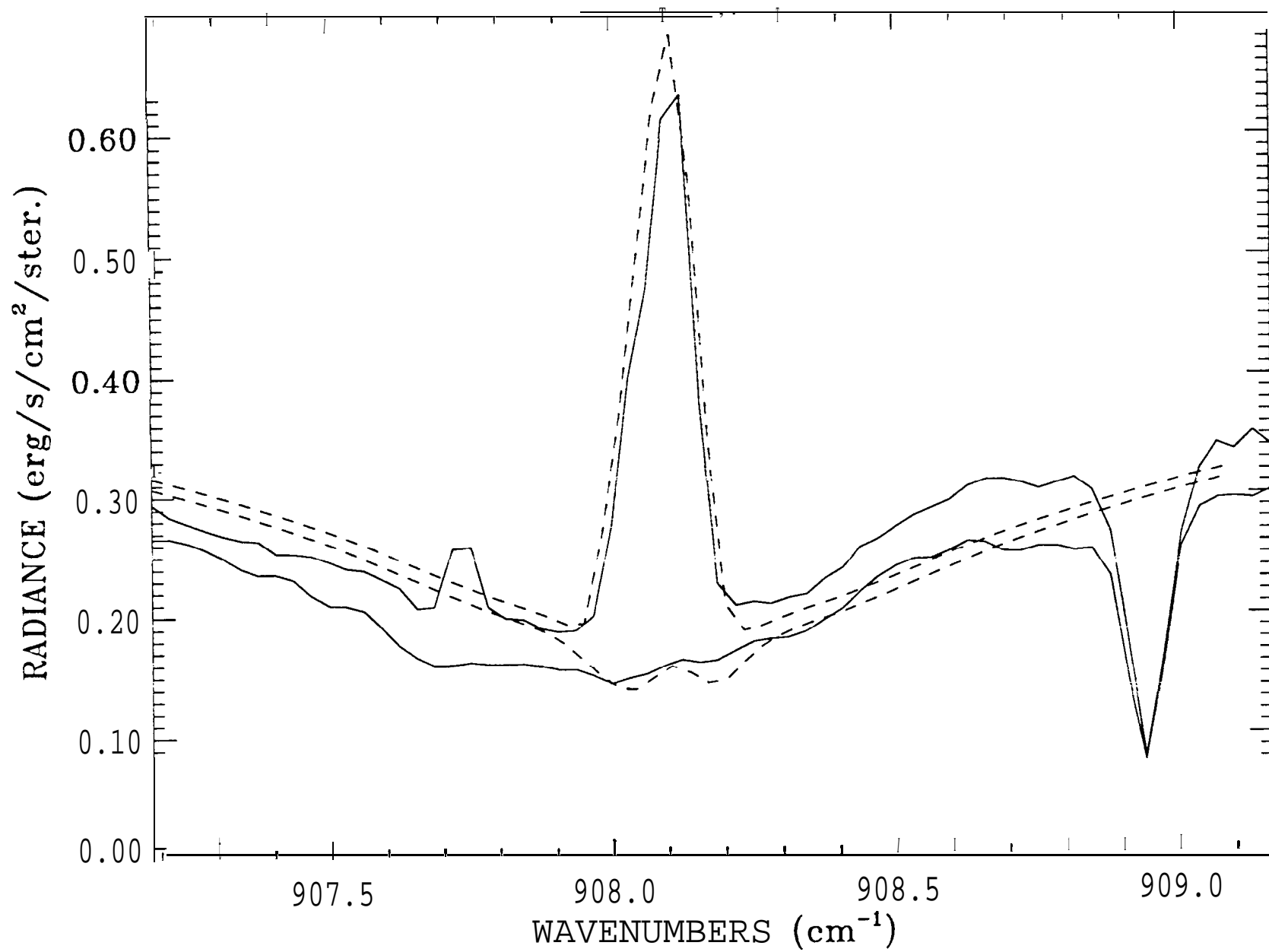
1994 Aug 6  
251° W

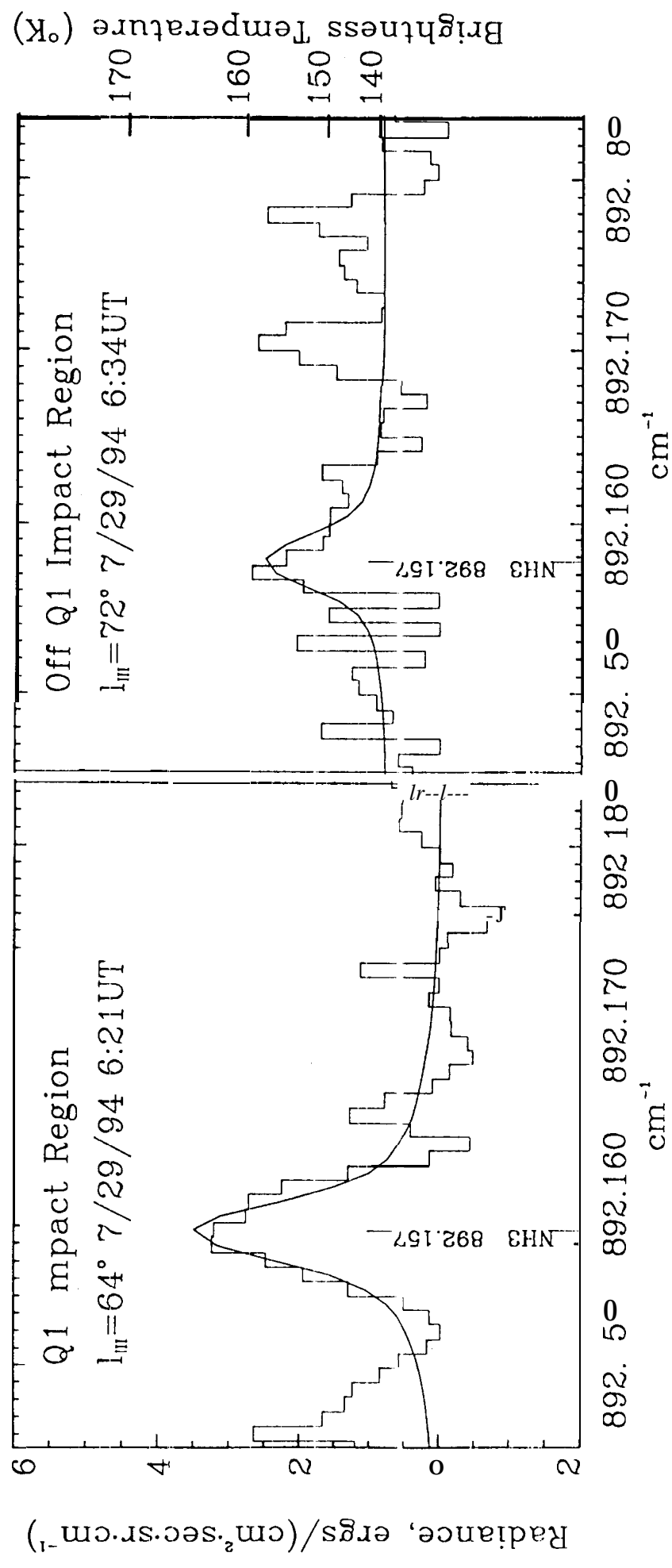


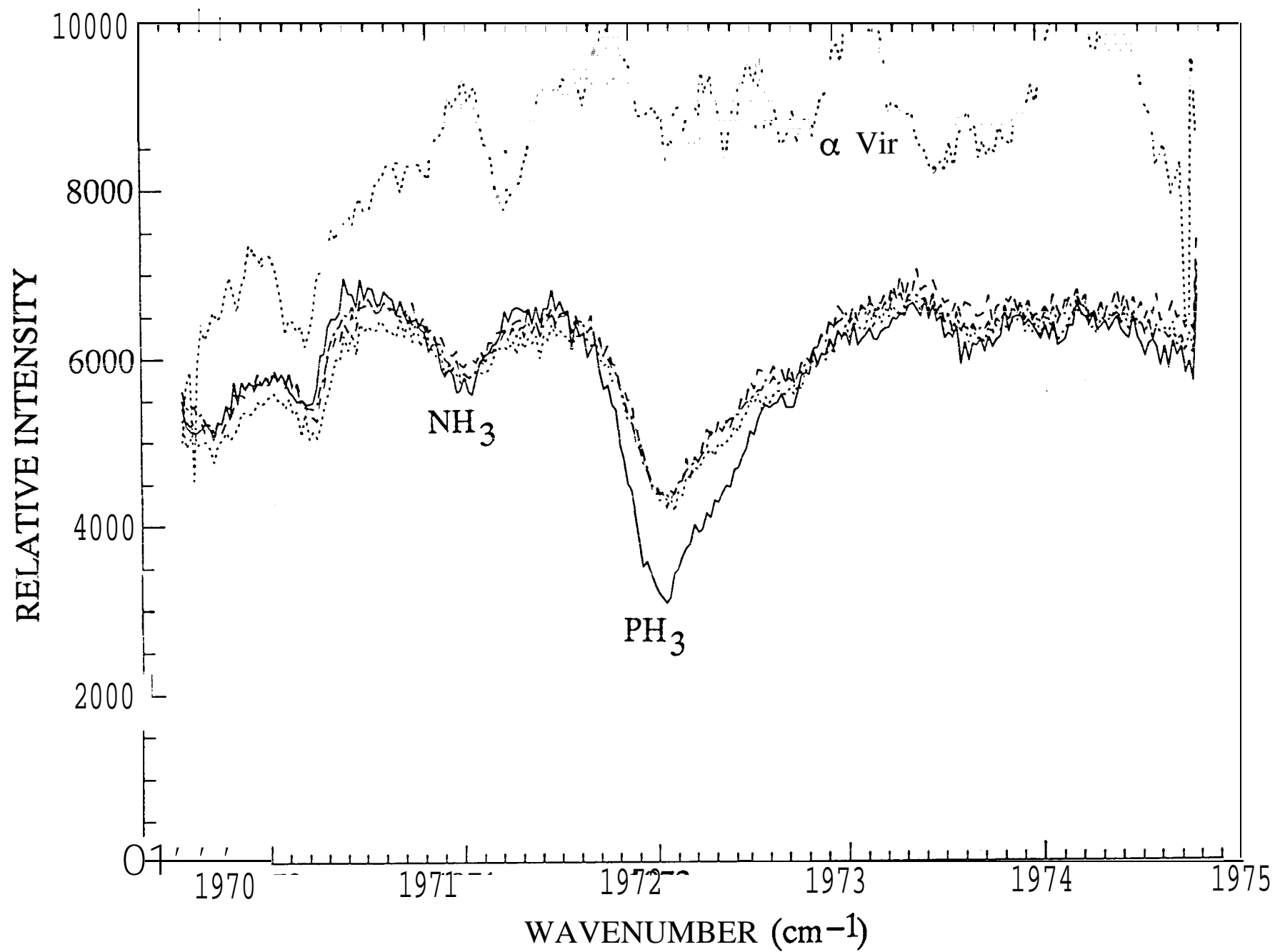
1994 Aug 6  
267° W

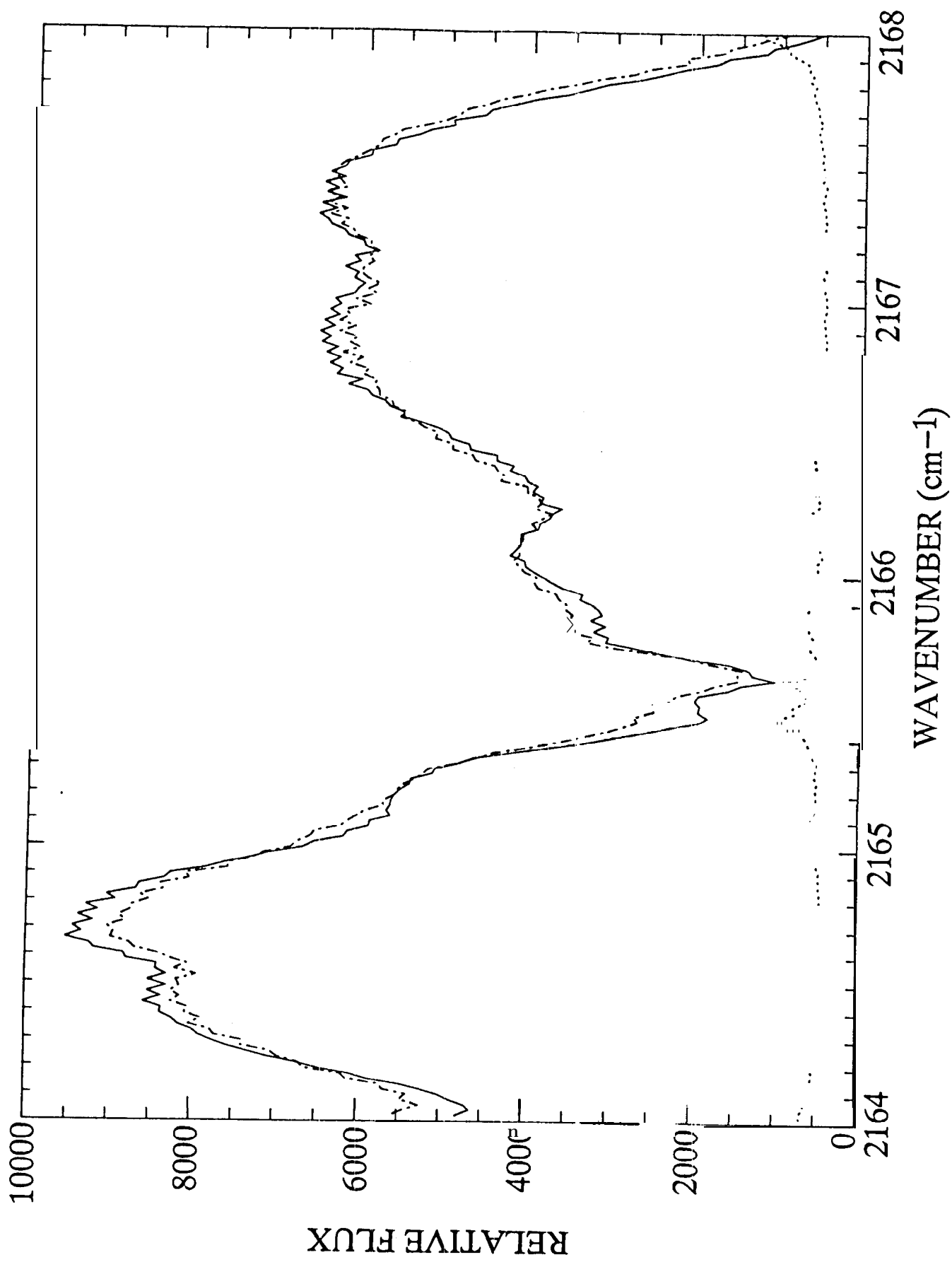




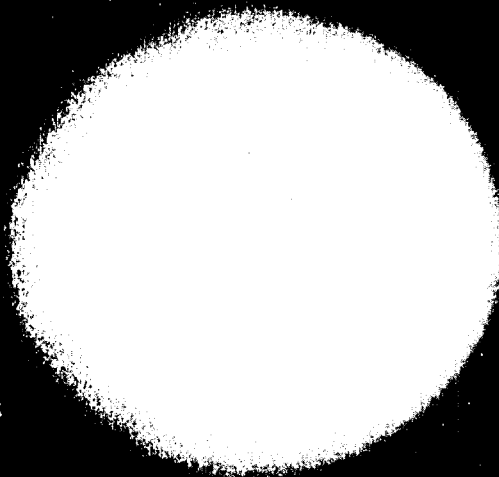






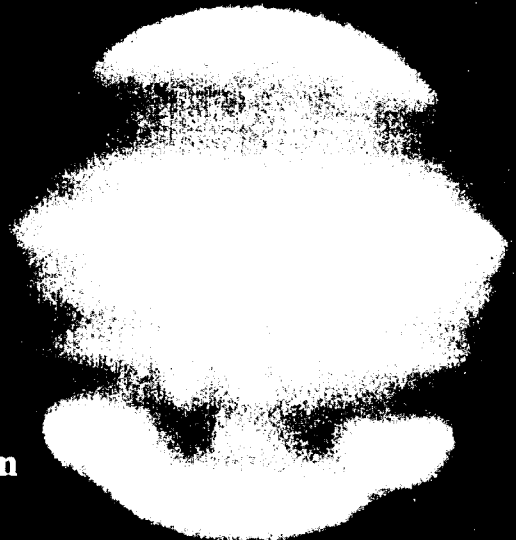


1.60 $\mu$ m



W K C A E

2.10 $\mu$ m



W K C A E

2.27 $\mu$ m



3.41 $\mu$ m





Jul 27

K C A E

Jul 28

G L K

Aug 3

K C A E

Aug 7

L K C